SAND2023-01657J

Controllable Phase Transition Properties in VO_2 Films via Metal-ion Intercalation

Zihao He[‡,1], *Zhimin Qi*[‡,2], *Bo Yang*[2], *Ping Lu*[3], *Jianan Shen*[2], *Neil R. Dilley*[4], *Xinghang Zhang*[2], *Haiyan Wang*[1,2*]

[1]School of Electrical and Computer Engineering, Purdue University, West Lafayette, IN 47907, USA

[2]School of Materials Engineering, Purdue University, West Lafayette, IN 47907, USA

[3]Sandia National Laboratories, Albuquerque, NM, 87185, USA

[4]Birck Nanotechnology Center, Purdue University, West Lafayette, IN 47907, USA

[‡]Zihao He and Zhimin Qi contributed equally to this work.

*Author to whom correspondence should be addressed. E-mail: hwang00@purdue.edu

KEYWORDS: VO_2, lithiation, transition temperature tuning, structural deformation, charge carrier density

ABSTRACT

VO_2 has shown great promise for sensors, smart windows, and energy storage devices, because of its drastic semiconductor-to-metal transition (SMT) near 340 K coupled with a structural transition. To push its application towards room temperature, effective transition temperature (T_c) tuning in VO_2 is desired. In this study, tailorable SMT characteristics in VO_2 films have been achieved by the electrochemical intercalation of foreign ions (e.g., Li-ions). By controlling the relative potential with respect to Li/Li^+ during the intercalation process, T_c of VO_2 can be effectively and systematically tuned in the window from 326.7 K to 340.8 K. The effective T_c tuning could be attributed to the observed strain and lattice distortion, and the change of the charge carrier density in VO_2 upon the intercalation process. This demonstration opens up a new approach in tuning the VO_2 phase transition towards room temperature device applications and enables future real-time phase change property tuning.

Semiconductor-to-metal transition (SMT) in oxides has attracted extensive research interests because of significant functional property changes and potential device applications.[1–5] In particular, vanadium dioxide (VO_2) has been widely studied as a strongly correlated Mott insulator.[6] VO_2 exhibits an intriguing metal-insulator switching upon cooling near 340 K (67 °C). The ultrafast and reversible first-order phase transition is coupled with a structural transition from rutile to monoclinic upon cooling.[7,8] In order to push the application of VO_2 towards room temperature, recent efforts have been devoted to the demonstration of transition temperature (T_c) tuning for VO_2 in a broad range. Among all, strain engineering and metallic doping are two common approaches. T_c of VO_2 films can be systemically tailored from 290 K to 340 K depending on the lattice-misfit strain,[9,10] and from 308 K to 384 K depending on the dopant selection.[11–14] However, high defect density inevitably deteriorates the overall phase transition properties.[15,16] Recently, a metal-VO_2 nanocomposite design has been demonstrated to mitigate such degradation.[17,18] T_c tuning for VO_2 films was achieved by the energy band structure reconstruction at the metal/VO_2 junction. However, most of these T_c tuning methods are based on as-deposited thin films and the demonstrations on post-deposition T_c tuning are limited.

To demonstrate T_c tuning for post-deposition samples, in this study, we adopt the electrochemical intercalation of Li-ions as a novel platform for tailoring the SMT characteristics in VO_2 films. It is interesting to note that VO_2 can be integrated as a cathode material in Li-ion batteries due to its unique layered structure.[19–21] Previous first-principle calculation of Li intercalation in VO_2(B) reveals possible intercalation sites and diffusion paths at different Li concentrations.[21,22] We thus hypothesize that a controllable SMT characteristics tuning in VO_2 films could be realized by varying Li concentration during the Li-ion intercalation process. The conceptual schematic of the intercalation process and the proposed mechanism is presented in

Figure 1a. During the discharging process, Li-ions can intercalate into the VO_2 cathode to form Li_xVO_2. **Figure 1b** illustrates the electric potential profiles of VO_2(B) with different intercalation strategies, and VO_2(M) shows similar features. ΔV represents the potential difference when the cell is discharged. Therefore, the 3V lithiated VO_2 film indicates a smaller potential difference than that of the 2V lithiated VO_2 film. VO_2 is known to have several polymorphs.[23,24] Specifically, VO_2(B) is selected due to its bilayer structure which consists of corner-sharing VO_6 octahedra.[25] Such layered structure provides two-dimensional planes for effective diffusion of Li-ions during charge/discharge cycling.[20,21] VO_2(M) is also selected because the distorted VO_6 octahedra share edges to create similar tunnel structure for Li-ion transport.[26,27] Compared to the structure of VO_2(B), a denser tunnel in VO_2(M) is supposed to achieve more significant structural deformation and consequently better T_c tuning. Previous structural study during cycling *via* in-situ approaches reveals reversible change of crystalline structure and oxidation state of V in the cutoff voltage window from 2.0 to 3.6 V.[22] Li intercalation in other 2D material candidates (e.g. MoS_2) reveals the significant improvement of electrical conductivity because of carrier injection.[28] Here, the microstructural, optical, and electrical characterizations reveal possible mechanisms for the T_c tuning upon lithiation. This study provides a promising platform for VO_2-based novel electronics and photonics with potential for real-time electrical and optical properties tuning.

In order to investigate the tuning effect of lithiation in VO_2 films by varying Li concentration, the electrical resistivity variation during the phase transition is characterized for the pristine, 3V, and 2V lithiated VO_2 films, i.e., VO_2(B) films on SRO-buffered STO substrates and VO_2(M) films on AZO-buffered sapphire substrates. The experimental section is discussed in the supporting information. The resistivity of the individual VO_2 layers are calculated by considering VO_2/SRO or VO_2/AZO as parallel resistors. The detailed measurement was reported elsewhere.[10] **Figure 2a1** and **b1** present the normalized electrical resistivity, $\rho = \rho(T)/\rho(270\,K)$, of the pristine and lithiated VO_2(B) and VO_2(M) films as a function of temperature. Compared to the resistivity transition curves of the pristine VO_2(B) and VO_2(M) films, the curves of 3V and 2V lithiated VO_2(B) and VO_2(M) films all shift towards the lower temperature side. Interestingly, the 2V lithiated VO_2(M) film shows an irregular ρ-T curve. The bump in the curve is likely because of the inhomogeneous phase transition within the VO_2 film, i.e., both metallic and insulating phases coexist in an inhomogeneous transitional state. Similar irregular transition (e.g. more than one endothermic/exothermic peak during the heating/cooling cycle) has been previously reported, which was attributed to the dispersive size distribution of $Ti_xV_{1-x}O_2$[26] or percolated Pt nanoparticles in VO_2 films in the previous cases.[29] The underlying mechanism will be discussed in detail in a later section. It is possibly due to irregular percolation of switchable metallic domains resulted from partial intercalation within the VO_2 matrix. To study other SMT characteristics (e.g. transition amplitude (ΔA), transition sharpness (ΔT), and the width of thermal hysteresis (ΔH)), the derivation of $log_{10}(\rho)$ vs. temperature of each sample is calculated based on the resistivity transition curves, as presented in **Figure 2a3-5** and **b3-5**. The comparison of T_c and ΔH is summarized in **Figure 2a2** and **b2**. Based on the previous VO_2 electrochemical studies, 2V corresponds to a higher potential difference ΔV and thus a higher Li intercalation amount to $Li_{1.0}VO_2$. In comparison, 3V corresponds to a lower potential difference ΔV and thus a lower Li intercalation amount to $Li_{0.5}VO_2$. Therefore, the electric potential here can be correlated to the introduced Li concentration.[21,30,31] T_c of both lithiated VO_2(B) and VO_2(M) films obviously reduces compared to that of their pure VO_2 counterparts, indicating an evident downward T_c tuning with the intercalation of Li-ions. Interestingly, T_c of VO_2(M) films shows more significant decrease than that of VO_2(B). In particular, the lowest T_c is achieved in 2V lithiated VO_2(M) film, which is 13.6 K lower than the corresponding pure VO_2(M) film.

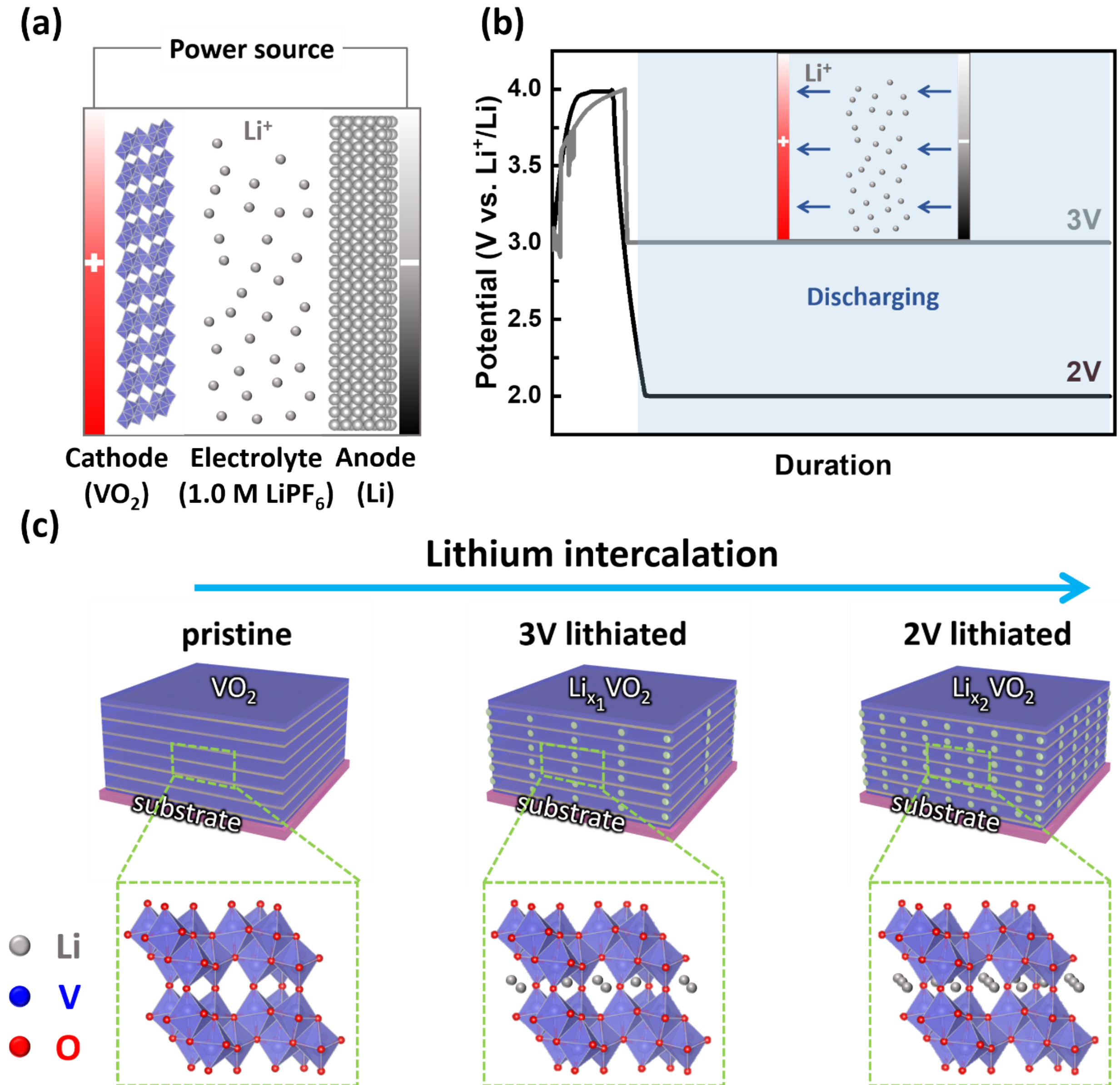

Figure 1. Schematic illustration of the Li-ion intercalation process in VO_2 films. (a) The operating mechanism of the electrochemical intercalation. Li-ions are intercalated into the VO_2 cathode during the discharging process. (b) The electric potential profiles of VO_2(B) with different intercalation strategy. ΔV represents the potential difference when the cell is discharged. Therefore, 3V lithiated VO_2 film indicates a smaller potential difference as compared to 2V

lithiated VO_2 film. (c) A proposed intercalation strategy of Li-ions in the VO_2 lattice to form Li_xVO_2. The enlarged schematics illustrate the crystal structure of VO_2(B) and the available intercalation sites for Li-ions. Because of smaller potential difference, 3V lithiated VO_2 film is supposed to intercalate less Li-ions as compared to 2V lithiated VO_2 film.

It is interesting to note that other SMT characteristics (e.g., ΔA, ΔT, and ΔH) exhibit different trends in VO_2(B) and VO_2(M) films. The comparison was summarized in **Figure S1** and **Table S1**. In the case of VO_2(B) films, both ΔA and ΔT prove no distinct degradation after the intercalation, while ΔH displays a minor increase. The wider thermal hysteresis implies the size reduction of crystalline domains after the Li-ion intercalation.[32] On the other hand, in the case of VO_2(M) films, ΔA slightly decreases while ΔT and ΔH obviously increase. The deterioration of the amplitude and the broadening of the transition width are both attributed to the increase of defect content (e.g., point defects, dislocations, grain boundaries, etc.) after the intercalation of Li-ions,[33] and the wider thermal hysteresis is related to smaller domains as discussed previously. To summarize, the Li-ion intercalation in both VO_2(B) and VO_2(M) films exhibits evident T_c tuning as well as other SMT characteristics. Such tuning effect can be further enhanced at higher Li concentration in the VO_2 lattice. In order to understand the underlying mechanisms of T_c tuning in **Figure 2**, the microstructural, optical, and electrical transport characterizations are illustrated in the following sections to study the change of strain state and the charge carrier density induced by Li-ion intercalation.

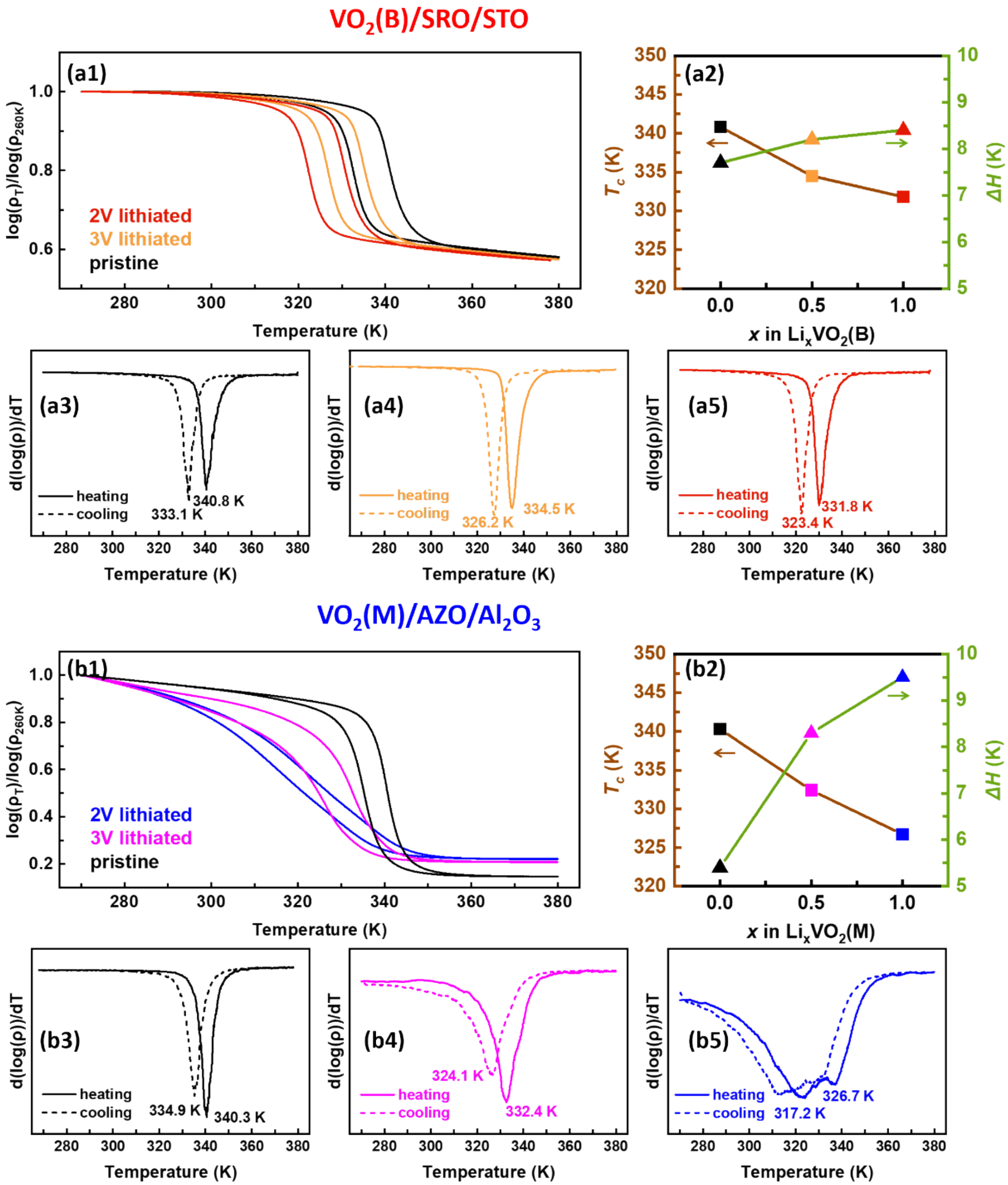

Figure 2. Electrical transport characterization. (a1) Normalized resistivity-temperature curve of the pristine, 3V, and 2V lithiated VO_2(B) films on SRO-buffer STO, respectively. (a2) The T_c and ΔH trend of VO_2(B) films as a function of electric potential. (a3-a5) Resistivity changing rate of the pristine, 3V, and 2V lithiated VO_2(B) films, respectively. (b1) Normalized resistivity-temperature curve of the pristine, 3V, and 2V lithiated VO_2(M) films on AZO-buffered c-cut

sapphire, respectively. (b2) The T_c and ΔH trend of VO_2(M) films as a function of electric potential. (b3-b5) Resistivity changing rate of the pristine, 3V, and 2V lithiated VO_2(M) films, respectively.

Microstructures of the pristine and lithiated VO_2(B) and VO_2(M) films are systematically characterized using XRD and cross-sectional STEM. Such microstructural characterizations provide essential strain information to probe the structural deformation induced by metal-ion intercalation. All the XRD θ-2θ spectra in **Figure 3a1** show one set of distinct VO_2(B) peaks corresponding to (00ℓ), revealing highly textured growth of VO_2(B) films along the c-axis on SRO-buffered STO substrates. The existence of a minor peak at around 37.8° is noted, as enlarged in **Figure S2**. The minor peak marked as * is considered as VO_2(M) $(20\bar{2})$ peak, which agrees with the prior study of the textured VO_2(B) growth on STO substrate, in which a small amount of VO_2(M) can co-grow in the VO_2(B) film when the film thickness exceeds a threshold.[34] **Figure 3a3** depicts the stack structure of VO_2(B)/SRO/STO. The sharp interface between VO_2(B) film and SRO buffer is observed without obvious inter-diffusion. To explore the change of strain state in VO_2(B) films before and after intercalation, a local XRD θ-2θ spectra near VO_2(B) (003) peak is shown in **Figure 3a2**. There is no obvious shift of VO_2(B) (003) peak before and after intercalation, indicating that limited strain is introduced upon Li-ion insertion. Hence a more localized lattice distortion analysis is required, which will be discussed in more details in the next section.

On the other hand, in the case of the pristine and lithiated VO_2(M) films, all the XRD θ-2θ spectra in **Figure 3b1** show one set of distinct VO_2(M) peaks corresponding to (00ℓ), revealing highly textured growth of VO_2(M) films along the c-axis on AZO-buffered sapphire substrates. AZO buffer layer is selected because of its lattice matching relationship with VO_2(M), and the deposition parameters from previous studies are utilized to minimize the interface roughness.[10]

The STEM image in **Figure 3b3** depicts the stack structure of VO_2(M)/AZO/Al_2O_3. It is noted that the AZO layer has a relatively rough top surface with some columnar feature. Such columnar growth of AZO films was reported previously under high oxygen partial pressure,[35] and the roughness on the top surface won't have significant impact on the overall resistivity as the film is relatively thin and serves as a bottom electrode. A local XRD θ-2θ spectra near VO_2(M) (002) peak (**Figure 3b2**) demonstrate the strain effect in VO_2(M) films before and after intercalation. The peak position of VO_2(M) (002) gradually shifts away from the bulk reference at high Li concentration. The result provides clear evidence of the tensile strain build-up along the c-axis upon Li-ion insertion in the VO_2(M) lattice. On the basis of the XRD results, the out-of-plane tensile strains are calculated as 0.31%, 0.52%, and 0.66% for the pristine, 3V, and 2V lithiated VO_2(M) films, respectively.

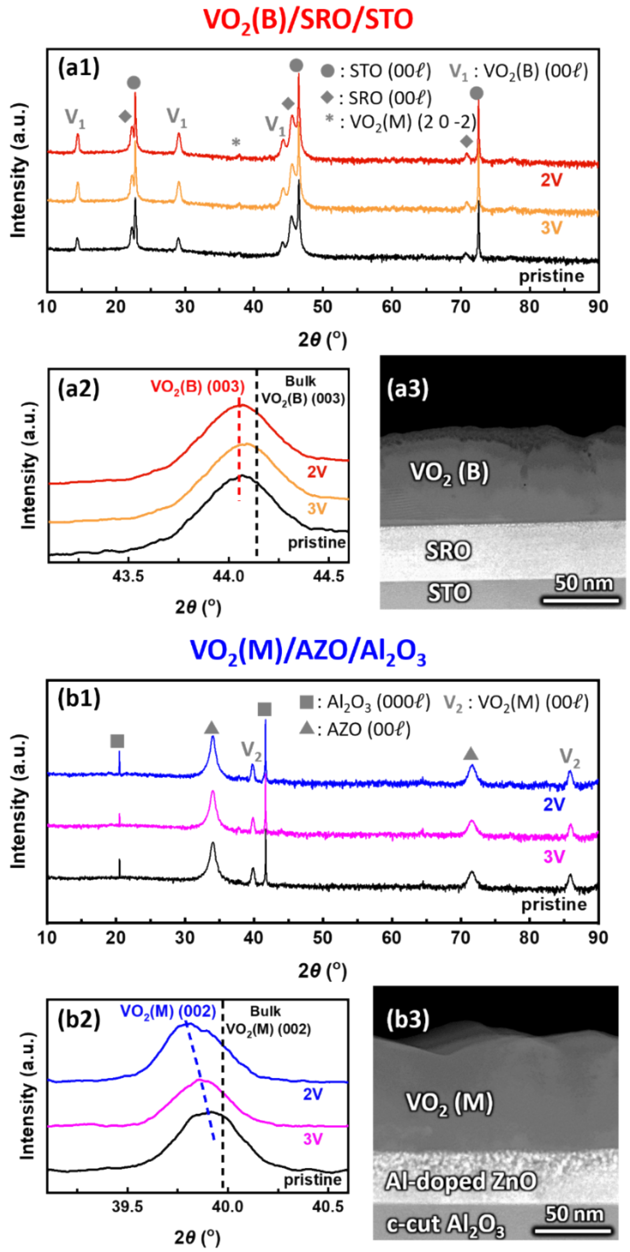

Figure 3. Microstructural characterization. (a1) XRD *θ-2θ* spectra of the pristine, 3V, and 2V lithiated VO_2(B) films on SRO-buffered STO substrates. (a2) Local scans near the VO_2(B) (003) peak to show the strain within the film. The black dashed line represents the bulk VO_2(B) (003) peak position (≈ 44.14°). (a3) Cross-sectional STEM image of VO_2(B) film on SRO-buffered STO substrate. (b1) XRD *θ-2θ* spectra of the pristine, 3V, and 2V lithiated VO_2(M) films on AZO-buffered c-cut sapphire substrates. (a2) Local scans near the VO_2(M) (002) peak to show the strain

within the film. The black dashed line represents the bulk VO_2(M) (002) peak position (≈ 39.97°). (a3) Cross-sectional STEM image of VO_2(M) film on AZO-buffered c-cut sapphire substrate.

In order to reveal the local lattice distortion in VO_2(B) films, GPA analysis is conducted on atomic-scale STEM images in **Figure 4**. The corresponding in-plane (ε_{xx}) and out-of-plane (ε_{yy}) lattice strain mappings are presented in **Figure 4 a2-3**, **b2-3**, and **c2-3** for the pristine and lithiated VO_2(B) films, respectively. Here, the lower part of the films is selected in each ε_{yy} mapping as the reference lattice. No obvious change of ε_{xx} is observed upon Li-ion insertion, indicating minimal in-plane lattice distortion. On the contrary, the bright yellow contrast in ε_{yy} mappings suggests a larger out-of-plane d-spacing compared to the reference lattice, i.e., a large out-of-plane lattice expansion in the upper film upon Li-ion insertion. In addition, a sharper change of ε_{yy} can be evidently observed at higher Li concentration, indicating the gradual increase in tensile strain along the c-axis upon Li-ion insertion in the VO_2(B) lattice. It is also noted that there is a very thin stripe in the top region of **Figure 4c2** and **4c3**. Such thin stripe is likely due to the scanning registration error during the STEM imaging process. Interestingly, major strain accumulation is seen within the upper film, suggesting that the Li-ion intercalation occurs more obviously in the top layer of the film (~18 nm). The intercalation nonuniformity is possibly because of the dense VO_2(B) film. As shown in **Figure S3**, The TEM comparison of the pristine and the 3V lithiated VO_2(B) films also confirms an increase of grain boundaries after the intercalation. These observations confirm the existence of localized structural/phase change and lattice distortion of VO_2(B) lattice during the intercalation process. Although XRD scans cannot depict obvious shift of VO_2(B) peaks before and after intercalation, the GPA analysis does illustrate local lattice distortion within the film. The seemingly contradictory results are due to the fact that X-ray penetrates through the entire film thickness and scans a large area, while cross-sectional HRSTEM images focus on a much-refined region within the film.

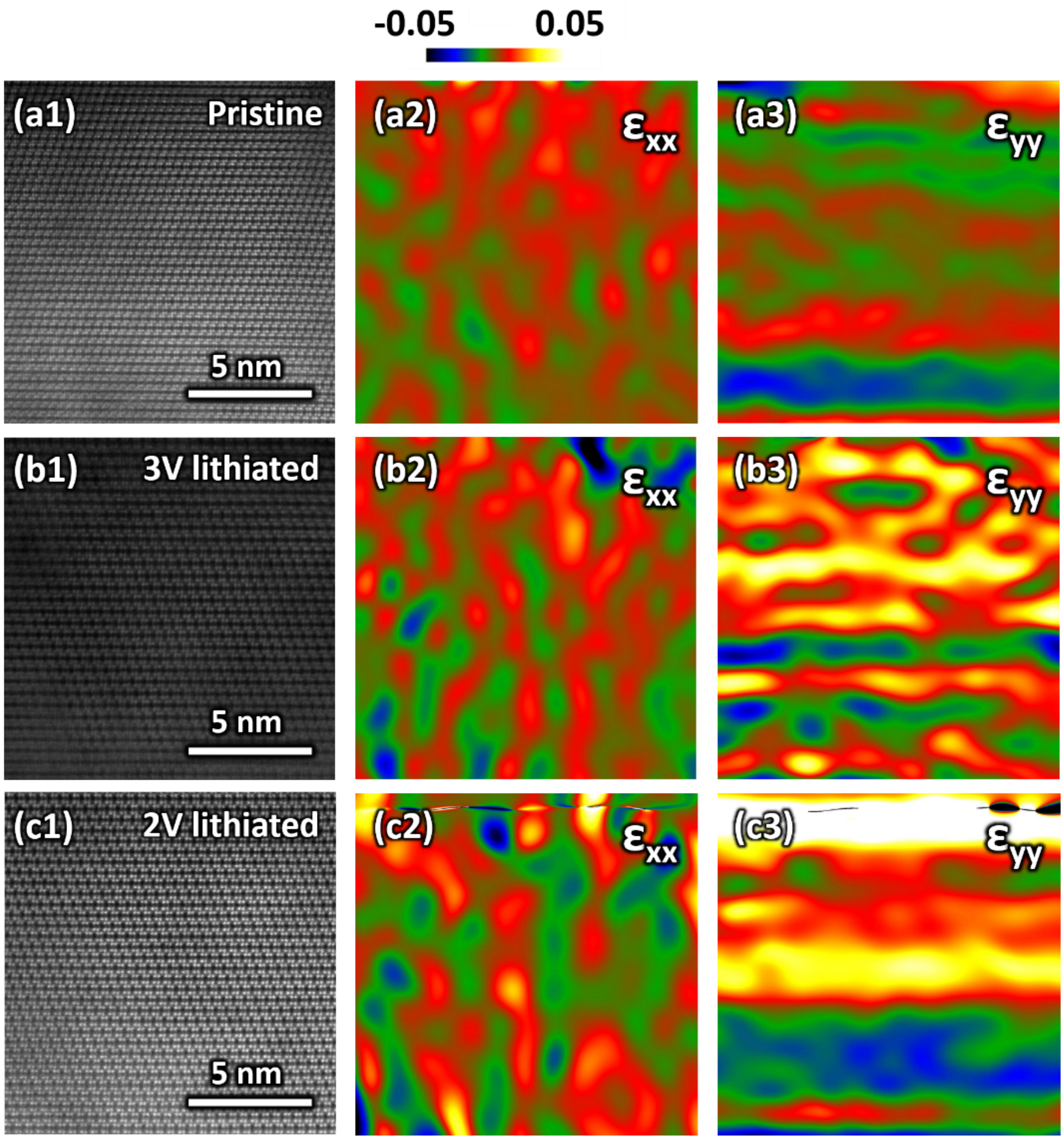

Figure 4. Atomic-scale microstructural characterization of VO_2(B) films on SRO-buffered STO substrates. (a1) Cross-sectional HR-STEM image of the pristine VO_2(B) film. The corresponding geometric phase analysis (GPA) (a2) in-plane strain (ε_{xx}) and (a3) out-of-plane stain (ε_{yy}) maps. (b1-b3) Cross-sectional HR-STEM image of the 3V lithiated VO_2(B) film and the corresponding

ε_{xx} and ε_{yy} maps. (c1-c3) Cross-sectional HR-STEM image of the 2V lithiated VO_2(B) film and the corresponding ε_{xx} and ε_{yy} maps.

Overall, the microstructural characterization offers essential evidence to investigate the strain accumulation and the localized structural deformation during the metal-ion intercalation process. In particular, VO_2(M) films exhibit obvious tensile strain build-up along the c-axis upon Li-ion insertion. On the contrary, VO_2(B) films exhibit a more localized lattice distortion upon Li-ion insertion, especially within the upper film. Based on the theoretical calculation, the insertion of Li-ions elongates the c-axis lattice and eliminates the alternating short and long V-V pair separations, i.e., the Li-ion intercalation drives the lattice towards the rutile configuration.[36] Thus the lattice expansion stabilizes the metallic phase and consequently triggers the T_c decrease.[37] Further, such structural evolution is reversible in the cutoff voltage window from 2.0 to 3.6 V.[22] As a result, such strain accumulation or structural deformation in both VO_2(M) and VO_2(B) films.

Considering the potential change of charge carrier density induced by Li-ion intercalation, the electrical transport and optical properties of the pristine and lithiated VO_2(B) and VO_2(M) films are systematically characterized using the Van der Pauw method and spectroscopic ellipsometry, respectively. A reliable Hall-effect measurement in VO_2 is challenging considering its low Hall mobility and the inhomogeneous nature of the SMT transition.[38] Here, the Hall effect for VO_2(M) films is evaluated in DC magnetic field of up to 9 T. As shown in **Figure S4a-c**, the Hall voltage (V_H) as a function of magnetic field (B) is measured at 380 K to diminish the effect of AZO buffer layer. For either pristine or lithiated VO_2(M) films, the negative sign of V_H implies that electrons are the major carriers to the transport at the metallic phases, which is consistent with prior studies of bulk VO_2.[38–40] The carrier density $n = -1/(R_H e)$, and the Hall mobility $\mu = R_H/\rho$ are illustrated in **Figure S4d**, where the Hall coefficient (R_H) is determined from the slopes of V_H vs.

B curves. It is clear that the charge carrier density almost doubles from $1.23 \times 10^{23}\ cm^{-3}$ (pristine) to $2.27 \times 10^{23}\ cm^{-3}$ (2V lithiated) when Li-ions immigrate through the tunnel structure in the VO_2(M) lattice. The calculated carrier density of the pristine film corresponds to 4.1 itinerant carriers per V ion, which agrees with previous reports of sputtered VO_2.[40] Although the Hall mobility reduces slightly at high Li concentration, the overall increase in the number of charge carriers can effectively suppress the SMT transition and consequently trigger the T_c decrease.

The optical absorption in the near-infrared, visible, and ultraviolet region are closely correlated with the charge carriers in the conduction band.[41,42] Therefore, the dielectric response of the pristine and lithiated VO_2(B) and VO_2(M) films is evaluated using angular dependent spectroscopic ellipsometry to explore the change of charge carrier density. The dielectric permittivity ε' (real part) at 25 °C and at 100 °C are shown in **Figure 5** for VO_2(B) and VO_2(M) films, respectively. The corresponding ε'' (imaginary part) is shown in **Figure S5**. In both VO_2(B) and VO_2(M) films, the values of ε' stay positive at 25 °C and become negative at 100 °C. Such optical response indicates the transition from low-temperature semiconducting behavior to metallic behavior, which is consistent with the electrical resistivity switching in **Figure 2**. At room temperature, the values of ε' decrease with the intercalation of Li-ions, indicating the injection of a large amount of charge carriers due to Li-ion diffusion. In particular, VO_2(M) films exhibit an overall decrease of ε' in the Uv-Vis-NIR region. The dense diffusion tunnel in VO_2(M) yields more significant electron doping effect and consequently better optical tuning at RT.[43] However, the inferior optical performance of VO_2(M) film at 100 °C (i.e., smaller ε' difference compared to VO_2(B)) is likely due to the inhomogeneous phase transition, as depicted in **Figure 4**. On the other hand, the tuning effect of Li-ion intercalation at 100 °C is characterized via epsilon-near zero (ENZ) wavelength. At the metallic phase, higher Li concentration leads to the shift of ENZ to the high-frequency region. The blueshift of ENZ wavelength reveals the increase of carrier density upon Li-ion insertion, which is consistent with the abovementioned Hall-effect measurement. Overall, the electrical transport and optical characterizations provide essential evidence to reveal the injection of a large amount of charge carriers in VO_2(B) and VO_2(M) films during the intercalation process. As previously reported in VO_2 nanobeams, the excess electrons could stabilize the metallic phase at lower temperature by weakening the V−V bonding and reducing the stabilization energy during the structural transformation.[44,45] Li intercalation in other 2D material candidates (e.g. MoS_2) reveals the significant improvement of electrical conductivity because of carrier injection.[28] As a result, the increase of charge carrier density upon Li-ion insertion in both VO_2(B) and VO_2(M) effectively suppresses the SMT transition and consequently triggers the T_c decrease.

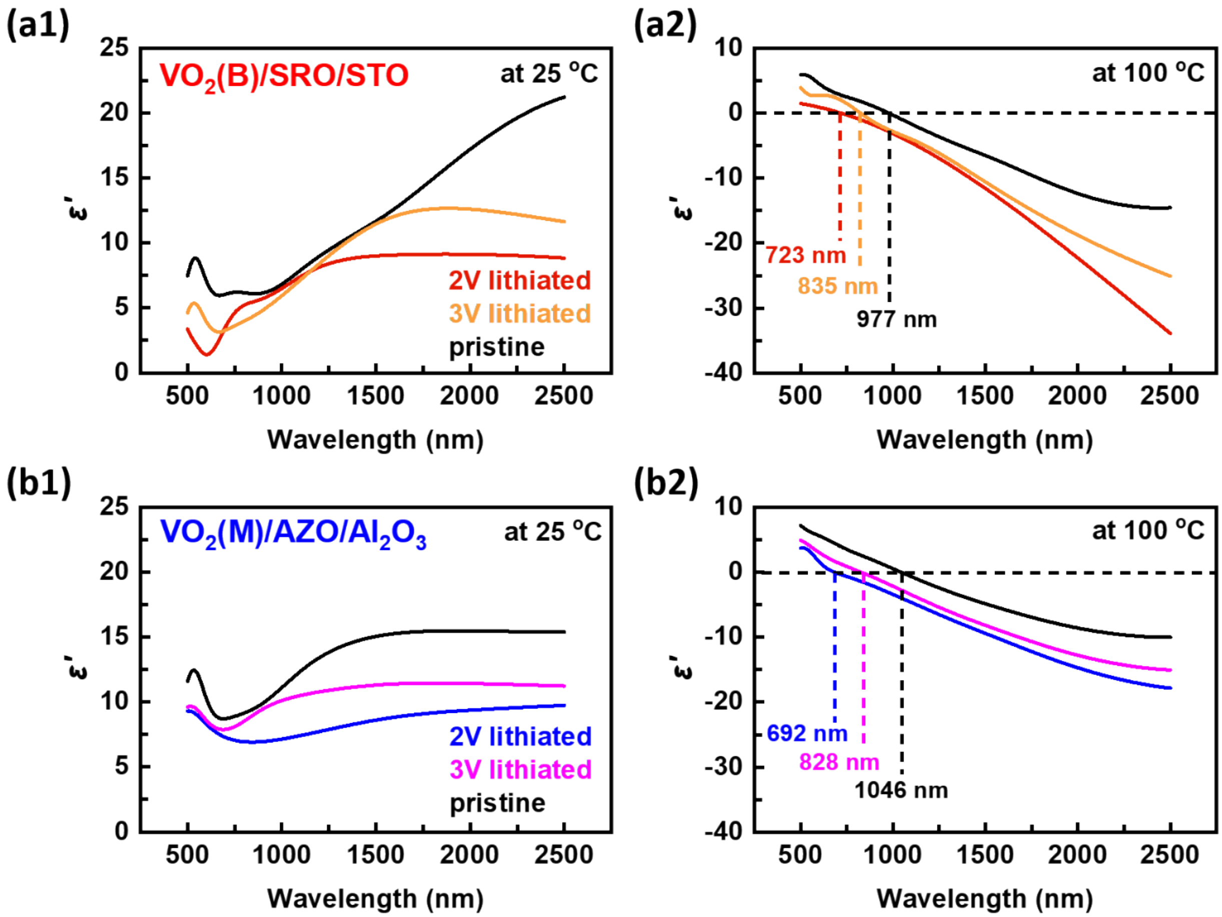

Figure 5. Optical characterization. The dielectric permittivity ε' (real part) (a1) at 25 °C and (a2) at 100 °C for the pristine, 3V, and 2V lithiated VO_2(B) films. The dielectric permittivity ε' (real part) (b1) at 25 °C and (b2) at 100 °C for the pristine, 3V, and 2V lithiated VO_2(M) films. The inset numbers represent the ENZ wavelengths for corresponding samples.

Compared to other SMT characteristics tuning approaches,[10,46–49] the electrochemical intercalation of Li-ions in this study demonstrates a simple and straightforward approach for effective T_c tuning in a broad range via electric potential control. In the meantime, the metal-ion intercalation approach sustains high quality VO_2 films with reasonable transition characteristics after the intercalation. Previous studies on Li/Zn/H-ion intercalation in VO_2 and other materials (e.g. MoS_2, Bi_2Se_3, graphite, etc.) gives some insights into the possible structural and properties change during the intercalation process.[28,37,51–53] The evolution of the lattice strain in Zn/VO_2 battery during the discharging/charging cycles was indicated by Rietveld refinement,[51] and the structural defects and strain accumulation in lithiated MoS_2 was characterized by AFM and Raman spectroscopy.[28] Both studies revealed the expansion/shrinkage of the lattice (i.e., structural deformation) induced upon proton insertion/extraction. Such structural deformation can suppress the SMT transition and stabilize the metallic rutile phase.[37] With respect to other physical properties change, the improved optical transparency and electrical conductivity were observed in Li-ion intercalated MoS_2,[28] Cu-ion intercalated Bi_2Se_3,[52] and Li-ion intercalated graphite,[53] respectively.

The tunnel structures in both VO_2(B) and VO_2(M) can potentially accommodate mass metal-ion intercalation. Taking advantage of the novel electrochemical platform for Li-ion intercalation, T_c of VO_2(B) and VO_2(M) films can be systemically tailored from 326.7 K to 340.8 K. The novelty of this work lies in that the Li-ion intercalation approach demonstrates the feasibility of systemic T_c tuning in VO_2(B) and VO_2(M) films for the first time. The observed structural deformation and the change of charge carrier density provide possible explanations for T_c tuning and shed insights on VO_2-based electronics and photonics towards room temperature applications. While further investigations are under way to quantify the more dominant factor, we argue that the change in carrier density can be more dominant in the case of VO_2(B). The GPA analysis suggests the existence of localized lattice distortion of VO_2(B) during the intercalation process, while the obvious peak shift in XRD was not observed. The result indicates limited impact from the global strain state change during the intercalation. Another intriguing future topic is to study the reversibility of Li intercalation, as other 2D material candidates (e.g. MoS_2) exhibits fully reversible discharge/charge cycle with little structural changes on the film edges.[28] Other metal-ion candidates, such as Zn-ions,[43,51] Al-ions,[54,55] and Mg-ions,[19,56] that have been previously demonstrated in battery cathode demonstrations, can also be explored. Metal-ion intercalation is a powerful method to dynamically engineer the physical properties of VO_2 and other layered materials, which opens up exciting opportunities in integrated electronics and optical devices with real-time property tuning.

In summary, the electrochemical intercalation of Li-ions has been demonstrated as a novel platform for T_c tuning in VO_2(B) and VO_2(M) films. During the discharging process, Li-ions can intercalate into the VO_2 cathode to form Li_xVO_2. By controlling the relative potential with respect to Li/Li^+ during the intercalation process, T_c of VO_2 is effectively and systematically tailored in the window from 326.7 K to 340.8 K. The mechanism of Li-ion induced T_c tuning is mainly attributed to two factors: the structural deformation and the change of charge carrier density. XRD and GPA analysis indicate the strain accumulation in VO_2(M) films and the lattice distortion in VO_2(B) films. Hall-effect measurement and spectroscopic ellipsometry reveal the injection of a large amount of charge carriers upon Li-ion insertion. Both factors stabilize the metallic phase and consequently lead to effective T_c decrease during the intercalation process. The capability to dynamically tailor the phase change properties via electrochemical intercalation method can be adopted in other layered oxides, which provides a promising approach towards the practical device applications of layered oxides in integrated electronics, optics, and sensors.

ASSOCIATED CONTENT

SUPPORTING INFORMATION

The Supporting Information is available free of charge at xxx.

- Additional experimental details, materials, and methods, the comparison of SMT characteristics, XRD, TEM, electrical, and optical properties of the pristine and lithiated VO_2(B) and VO_2(M) films

AUTHOR INFORMATION

Corresponding Author

Haiyan Wang – School of Electrical and Computer Engineering, Purdue University, West Lafayette, IN 47907, USA; School of Materials Engineering, Purdue University, West Lafayette, IN 47907, USA

Authors

Zihao He – School of Electrical and Computer Engineering, Purdue University, West Lafayette, IN 47907, USA

Zhimin Qi – School of Materials Engineering, Purdue University, West Lafayette, IN 47907, USA

Bo Yang – School of Materials Engineering, Purdue University, West Lafayette, IN 47907, USA

Ping Lu – Sandia National Laboratories, Albuquerque, NM 87185, USA

Jianan Shen – School of Materials Engineering, Purdue University, West Lafayette, IN 47907, USA

Neil R. Dilley –Birck Nanotechnology Center, Purdue University, West Lafayette, IN 47907, USA

Xinghang Zhang – School of Materials Engineering, Purdue University, West Lafayette, IN 47907, USA

AUTHOR CONTRIBUTIONS

H.W. conceived and supervised the project. H.W., X.Z., Z.H., and Z.Q. discussed the experimental design and project planning. Z.H. and Z.Q. contributed equally to the thin film fabrication, electrochemical intercalation, and characterization. B.Y. contributed to the electrochemical intercalation. P.L. contributed to the HRSTEM imaging. J.S. contributed to the TEM sample preparation. N.D. contributed to the electrical transport measurement. H.W., Z.H., and Z.Q. drafted and revised the manuscript. All authors have revised and given the approval for the final version of the manuscript. ‡Z.H. and Z.Q. contributed equally to this work.

Notes

The authors declare no competing financial interest.

ACKNOWLEDGEMENTS

The authors acknowledge the support from the U.S. National Science Foundation (DMR-1809520 for thin film deposition, structural and property characterizations and DMR-2016453 for high resolution TEM/STEM work). Z.Q., B.Y., J.S., and H.W. acknowledge the support from the Office of Naval Research (N00014-20-1-2600, N00014-22-1-2160, N00014-20-1-2043). Sandia National

Laboratories is a multi-program laboratory managed and operated by National Technology and Engineering Solutions of Sandia, LLC., a wholly owned subsidiary of Honeywell International, Inc., for the U.S. Department of Energy's National Nuclear Security Administration under contract DE-NA0003525. This paper describes objective technical results and analysis. Any subjective views or opinions that might be expressed in the paper do not necessarily represent the views of the U.S. Department of Energy or the United States Government.

REFERENCES

(1) Mott, N. F. Metal-Insulator Transition. *Rev. Mod. Phys.* **1968**, *40* (4), 677–683. https://doi.org/10.1103/RevModPhys.40.677.

(2) Kuwahara, H.; Tomioka, Y.; Asamitsu, A.; Moritomo, Y.; Tokura, Y. A First-Order Phase Transition Induced by a Magnetic Field. *Science* **1995**, *270* (5238), 961–963. https://doi.org/10.1126/SCIENCE.270.5238.961.

(3) Urushibara, A.; Moritomo, Y.; Arima, T.; Asamitsu, A.; Kido, G.; Tokura, Y. Insulator-Metal Transition and Giant Magnetoresistance in $La_{1-x}Sr_xMnO_3$. *Phys. Rev. B* **1995**, *51* (20), 14103. https://doi.org/10.1103/PhysRevB.51.14103.

(4) Imada, M.; Fujimori, A.; Tokura, Y. Metal-Insulator Transitions. *Rev. Mod. Phys.* **1998**, *70*, 1039.

(5) Kravchenko, S. V; Sarachik, M. P. Metal–Insulator Transition in Two-Dimensional Electron Systems. *Reports Prog. Phys.* **2003**, *67* (1), 1. https://doi.org/10.1088/0034-4885/67/1/R01.

(6) Morin, F. J. Oxides Which Show a Metal-to-Insulator Transition at the Neel Temperature. *Phys. Rev. Lett.* **1959**, *3* (1), 34.

(7) Goodenough, J. B. The Two Components of the Crystallographic Transition in VO_2. *J. Solid State Chem.* **1971**, *3* (4), 490–500. https://doi.org/10.1016/0022-4596(71)90091-0.

(8) Zylbersztejn, A.; Mott, N. F. Metal-Insulator Transition in Vanadium Dioxide. *Phys. Rev. B* **1975**, *11* (11), 4383–4395. https://doi.org/10.1103/PhysRevB.11.4383.

(9) Jeong, J.; Aetukuri, N.; Graf, T.; Schladt, T. D.; Samant, M. G.; Parkin, S. S. P. Suppression of Metal-Insulator Transition in VO_2 by Electric Field-Induced Oxygen Vacancy Formation. *Science* **2013**, *339* (6126), 1402–1405. https://doi.org/10.1126/SCIENCE.1230512/SUPPL_FILE/JEONG.SM.PDF.

(10) Jian, J.; Wang, X.; Li, L.; Fan, M.; Zhang, W.; Huang, J.; Qi, Z.; Wang, H. Continuous Tuning of Phase Transition Temperature in VO_2 Thin Films on c-Cut Sapphire Substrates via Strain Variation. *ACS Appl. Mater. Interfaces* **2017**, *9* (6), 5319–5327. https://doi.org/10.1021/ACSAMI.6B13217.

(11) Wang, N.; Liu, S.; Zeng, X. T.; Magdassi, S.; Long, Y. Mg/W-Codoped Vanadium Dioxide Thin Films with Enhanced Visible Transmittance and Low Phase Transition Temperature. *J. Mater. Chem. C* **2015**, *3* (26), 6771. https://doi.org/10.1039/c5tc01062d.

(12) Chen, B.; Yang, D.; Charpentier, P. A.; Zeman, M. Al^{3+}-Doped Vanadium Dioxide Thin Films Deposited by PLD. *Sol. Energy Mater. Sol. Cells* **2009**, *93* (9), 1550–1554. https://doi.org/10.1016/j.solmat.2009.04.005.

(13) Manning, T. D.; Parkin, I. P.; Blackman, C.; Qureshi, U. APCVD of Thermochromic

Vanadium Dioxide Thin Films-Solid Solutions $V_{2-x}M_xO_2$ (M = Mo, Nb) or Composites VO_2 : SnO_2. *J. Mater. Chem.* **2005**, *15* (42), 4560–4566. https://doi.org/10.1039/b510552h.

(14) Tan, X.; Liu, W.; Long, R.; Zhang, X.; Yao, T.; Liu, Q.; Sun, Z.; Cao, Y.; Wei, S. Symmetry-Controlled Structural Phase Transition Temperature in Chromium-Doped Vanadium Dioxide. *J. Phys. Chem. C* **2016**, *120* (49), 28163–28168. https://doi.org/10.1021/acs.jpcc.6b08586.

(15) Sayle, D. C.; Watson, G. W. Dislocations, Lattice Slip, Defects and Rotated Domains: The Effect of a Lattice Misfit on Supported Thin-Film Metal Oxides. *Phys. Chem. Chem. Phys.* **2000**, *2* (23), 5491–5499. https://doi.org/10.1039/b006587k.

(16) Jian, J.; Zhang, W.; Jacob, C.; Chen, A.; Wang, H.; Huang, J.; Wang, H. Roles of Grain Boundaries on the Semiconductor to Metal Phase Transition of VO_2 Thin Films. *Appl. Phys. Lett.* **2015**, *107* (10), 102105. https://doi.org/10.1063/1.4930831.

(17) Jian, J.; Wang, X.; Misra, S.; Sun, X.; Qi, Z.; Gao, X.; Sun, J.; Donohue, A.; Gen Lin, D.; Pol, V.; Youngblood, J.; Wang, H.; Li, L.; Huang, J.; Wang, H.; Jian, J.; Wang, X.; Misra, S.; Sun, X.; Qi, Z.; Gao, X.; Lin, D. G.; Pol, V.; Youngblood, J.; Wang, H.; Li, L.; Huang, J.; Sun, J.; Donohue A Woollam, A. J. Broad Range Tuning of Phase Transition Property in VO_2 Through Metal-Ceramic Nanocomposite Design. *Adv. Funct. Mater.* **2019**, *29* (36), 1903690. https://doi.org/10.1002/ADFM.201903690.

(18) He, Z.; Jian, J.; Misra, S.; Gao, X.; Wang, X.; Qi, Z.; Yang, B.; Zhang, D.; Zhang, X.; Wang, H. Bidirectional Tuning of Phase Transition Properties in Pt:VO_2 Nanocomposite Thin Films. *Nanoscale* **2020**, *12* (34), 17886–17894. https://doi.org/10.1039/D0NR04008H.

(19) Pei, C.; Xiong, F.; Sheng, J.; Yin, Y.; Tan, S.; Wang, D.; Han, C.; An, Q.; Mai, L. VO_2 Nanoflakes as the Cathode Material of Hybrid Magnesium-Lithium-Ion Batteries with High Energy Density. *ACS Appl. Mater. Interfaces* **2017**, *9* (20), 17060–17066. https://doi.org/10.1021/ACSAMI.7B02480/SUPPL_FILE/AM7B02480_SI_001.PDF.

(20) Niu, C.; Meng, J.; Han, C.; Zhao, K.; Yan, M.; Mai, L. VO_2 Nanowires Assembled into Hollow Microspheres for High-Rate and Long-Life Lithium Batteries. *Nano Lett.* **2014**, *14* (5), 2873–2878. https://doi.org/10.1021/NL500915B/SUPPL_FILE/NL500915B_SI_001.PDF.

(21) Li, S.; Liu, J. B.; Wan, Q.; Xu, J.; Liu, B. X. First-Principles Analysis of Li Intercalation in VO_2(B). *Chem. Mater.* **2017**, *29* (23), 10075–10087. https://doi.org/10.1021/ACS.CHEMMATER.7B03750/SUPPL_FILE/CM7B03750_SI_001.PDF.

(22) Liu, Q.; Tan, G.; Wang, P.; Abeyweera, S. C.; Zhang, D.; Rong, Y.; Wu, A. Y.; Lu, J.; Sun, C. J.; Ren, Y.; Liu, Y.; Muehleisen, R. T.; Guzowski, L. B.; Li, J.; Xiao, X.; Sun, Y. Revealing Mechanism Responsible for Structural Reversibility of Single-Crystal VO_2 Nanorods upon Lithiation/Delithiation. *Nano Energy* **2017**, *36*, 197–205. https://doi.org/10.1016/J.NANOEN.2017.04.023.

(23) Subba Reddy, C. V.; Walker, E. H.; Wicker, S. A.; Williams, Q. L.; Kalluru, R. R. Synthesis of VO_2 (B) Nanorods for Li Battery Application. *Curr. Appl. Phys.* **2009**, *9* (6), 1195–1198. https://doi.org/10.1016/J.CAP.2009.01.012.

(24) Leroux, C.; Nihoul, G.; Van Tendeloo, G. From VO2(B) to VO2(R): Theoretical Structures of VO_2 Polymorphs and in Situ Electron Microscopy. *Phys. Rev. B* **1998**, *57* (9), 5111.

https://doi.org/10.1103/PhysRevB.57.5111.

(25) Chernova, N. A.; Roppolo, M.; Dillon, A. C.; Whittingham, M. S. Layered Vanadium and Molybdenum Oxides : Batteries and Electrochromics. *J. Mater. Chem.* **2009**, *19* (17), 2526–2552. https://doi.org/10.1039/B819629J.

(26) Wu, Y.; Fan, L.; Liu, Q.; Chen, S.; Huang, W.; Chen, F.; Liao, G.; Zou, C.; Wu, Z. Decoupling the Lattice Distortion and Charge Doping Effects on the Phase Transition Behavior of VO_2 by Titanium (Ti4+) Doping. *Sci. Rep.* **2015**, *5* (1), 1–8. https://doi.org/10.1038/srep09328.

(27) Li, W.; Huang, J.; Cao, L.; Li, X.; Chen, S.; Feng, L. Polycrystalline VO_2(M) with Well-Dispersed Crystalline Zones for Enhanced Electroactivity of Lithium-Ion Batteries. *J. Alloys Compd.* **2020**, *812*, 152122. https://doi.org/10.1016/J.JALLCOM.2019.152122.

(28) Xiong, F.; Wang, H.; Liu, X.; Sun, J.; Brongersma, M.; Pop, E.; Cui, Y. Li Intercalation in MoS_2: In Situ Observation of Its Dynamics and Tuning Optical and Electrical Properties. *Nano Lett.* **2015**, *15* (10), 6777–6784. https://doi.org/10.1021/ACS.NANOLETT.5B02619/SUPPL_FILE/NL5B02619_SI_001.PDF.

(29) Jo, M.; Seo, Y. W.; Yoon, H.; Nam, Y. S.; Choi, S. Y.; Choi, B. J.; Son, J. Embedded Metallic Nanoparticles Facilitate Metastability of Switchable Metallic Domains in Mott Threshold Switches. *Nat. Commun.* **2022**, *13* (1), 1–9. https://doi.org/10.1038/s41467-022-32081-x.

(30) Chirayil, T. A.; Zavalij, P. Y.; Whittingham, M. S. A New Vanadium Dioxide Cathode. *J.*

Electrochem. Soc. **1996**, *143* (9), L193–L195. https://doi.org/10.1149/1.1837083/XML.

(31) Huang, J.; Wang, X.; Liu, J.; Sun, X.; Wang, L.; He, X. Flexible Free-Standing VO_2 (B) Nanobelt Films as Additive-Free Cathode for Lithium-Ion Batteries. *Int. J. Electrochem. Sci* **2011**, *6*, 1709–1719.

(32) Rozen, J.; Lopez, R.; Haglund, R. F.; Feldman, L. C. Two-Dimensional Current Percolation in Nanocrystalline Vanadium Dioxide Films. *Appl. Phys. Lett.* **2006**, *88* (8), 081902. https://doi.org/10.1063/1.2175490.

(33) Narayan, J.; Bhosle, V. M. Phase Transition and Critical Issues in Structure-Property Correlations of Vanadium Oxide. *J. Appl. Phys.* **2006**, *100* (10), 103524. https://doi.org/10.1063/1.2384798.

(34) Chen, A.; Bi, Z.; Zhang, W.; Jian, J.; Jia, Q.; Wang, H. Textured Metastable VO_2 (B) Thin Films on SrTiO3 Substrates with Significantly Enhanced Conductivity. *Appl. Phys. Lett.* **2014**, *104* (7), 071909. https://doi.org/10.1063/1.4865898.

(35) Lee, J. H.; Chou, C. Y.; Bi, Z.; Tsai, C. F.; Wang, H. Growth-Controlled Surface Roughness in Al-Doped ZnO as Transparent Conducting. *Nanotechnology* **2009**, *20* (39), 395704. https://doi.org/10.1088/0957-4484/20/39/395704.

(36) Warnick, K. H.; Wang, B.; Pantelides, S. T. Hydrogen Dynamics and Metallic Phase Stabilization in VO_2. *Appl. Phys. Lett.* **2014**, *104* (10), 101913. https://doi.org/10.1063/1.4868541.

(37) Shibuya, K.; Sawa, A. Modulation of Metal–Insulator Transition in VO_2 by Electrolyte Gating-Induced Protonation. *Adv. Electron. Mater.* **2016**, *2* (2), 1500131.

https://doi.org/10.1002/AELM.201500131.

(38) Rosevear, W. H.; Paul, W. Hall Effect in VO_2 near the Semiconductor-to-Metal Transition. *Phys. Rev. B* **1973**, *7* (5), 2109. https://doi.org/10.1103/PhysRevB.7.2109.

(39) Barker, A. S.; Verleur, H. W.; Guggenheim, H. J. Infrared Optical Properties of Vanadium Dioxide Above and Below the Transition Temperature. *Phys. Rev. Lett.* **1966**, *17* (26), 1286. https://doi.org/10.1103/PhysRevLett.17.1286.

(40) Ruzmetov, D.; Heiman, D.; Claflin, B. B.; Narayanamurti, V.; Ramanathan, S. Hall Carrier Density and Magnetoresistance Measurements in Thin-Film Vanadium Dioxide across the Metal-Insulator Transition. *Phys. Rev. B* **2009**, *79* (15), 153107. https://doi.org/10.1103/PHYSREVB.79.153107/FIGURES/4/MEDIUM.

(41) Tiwald, T. E.; Thompson, D. W.; Woollam, J. A.; Paulson, W.; Hance, R. Application of IR Variable Angle Spectroscopic Ellipsometry to the Determination of Free Carrier Concentration Depth Profiles. *Thin Solid Films* **1998**, *313–314*, 661–666. https://doi.org/10.1016/S0040-6090(97)00973-5.

(42) Schubert, M. Another Century of Ellipsometry. *Ann. Phys.* **2006**, *15* (7–8), 480–497. https://doi.org/10.1002/ANDP.200510204.

(43) Zhang, L.; Miao, L.; Zhang, B.; Wang, J.; Liu, J.; Tan, Q.; Wan, H.; Jiang, J. A Durable VO_2 (M)/Zn Battery with Ultrahigh Rate Capability Enabled by Pseudocapacitive Proton Insertion. *J. Mater. Chem. A* **2020**, *8* (4), 1731–1740. https://doi.org/10.1039/C9TA11031C.

(44) Griffiths, C. H.; Eastwood, H. K. Influence of Stoichiometry on the Metal-semiconductor

Transition in Vanadium Dioxide. *J. Appl. Phys.* **1974**, *45* (5), 2201. https://doi.org/10.1063/1.1663568.

(45) Zhang, S.; Kim, I. S.; Lauhon, L. J. Stoichiometry Engineering of Monoclinic to Rutile Phase Transition in Suspended Single Crystalline Vanadium Dioxide Nanobeams. *Nano Lett.* **2011**, *11* (4), 1443–1447. https://doi.org/10.1021/NL103925M/ASSET/IMAGES/LARGE/NL-2010-03925M_0004.JPEG.

(46) Mlyuka, N. R.; Niklasson, G. A.; Granqvist, C. G. Mg Doping of Thermochromic VO_2 Films Enhances the Optical Transmittance and Decreases the Metal-Insulator Transition Temperature. *Appl. Phys. Lett.* **2009**, *95* (17), 171909. https://doi.org/10.1063/1.3229949.

(47) Takahashi, I.; Hibino, M.; Kudo, T. Thermochromic Properties of Double-Doped VO_2 Thin Films Prepared by a Wet Coating Method Using Polyvanadate-Based Sols Containing W and Mo or W and Ti. *Jpn. J. Appl. Phys.* **2001**, *40* (3 A), 1391–1395. https://doi.org/10.1143/JJAP.40.1391/XML.

(48) Yang, M.; Yang, Y.; Hong, B.; Wang, L.; Hu, K.; Dong, Y.; Xu, H.; Huang, H.; Zhao, J.; Chen, H.; Song, L.; Ju, H.; Zhu, J.; Bao, J.; Li, X.; Gu, Y.; Yang, T.; Gao, X.; Luo, Z.; Gao, C. Suppression of Structural Phase Transition in VO_2 by Epitaxial Strain in Vicinity of Metal-Insulator Transition. *Sci. Rep.* **2016**, *6* (1), 1–10. https://doi.org/10.1038/srep23119.

(49) Lee, D.; Lee, J.; Song, K.; Xue, F.; Choi, S. Y.; Ma, Y.; Podkaminer, J.; Liu, D.; Liu, S. C.; Chung, B.; Fan, W.; Cho, S. J.; Zhou, W.; Lee, J.; Chen, L. Q.; Oh, S. H.; Ma, Z.; Eom, C. B. Sharpened VO_2 Phase Transition via Controlled Release of Epitaxial Strain. *Nano Lett.* **2017**, *17* (9), 5614–5619.

https://doi.org/10.1021/ACS.NANOLETT.7B02482/SUPPL_FILE/NL7B02482_SI_003.AVI.

(50) Fan, L. L.; Wu, Y. F.; Si, C.; Zou, C. W.; Qi, Z. M.; Li, L. B.; Pan, G. Q.; Wu, Z. Y. Oxygen Pressure Dependent VO_2 Crystal Film Preparation and the Interfacial Epitaxial Growth Study. *Thin Solid Films* **2012**, *520* (19), 6124–6129. https://doi.org/10.1016/j.tsf.2012.05.086.

(51) Li, Z.; Ganapathy, S.; Xu, Y.; Zhou, Z.; Sarilar, M.; Wagemaker, M.; Li, Z.; Ganapathy, S.; Xu, Y.; Zhou, Z.; Sarilar, M.; Wagemaker, M. Mechanistic Insight into the Electrochemical Performance of Zn/VO_2 Batteries with an Aqueous $ZnSO_4$ Electrolyte. *Adv. Energy Mater.* **2019**, *9* (22), 1900237. https://doi.org/10.1002/AENM.201900237.

(52) Yao, J.; Koski, K. J.; Luo, W.; Cha, J. J.; Hu, L.; Kong, D.; Narasimhan, V. K.; Huo, K.; Cui, Y. Optical Transmission Enhacement through Chemically Tuned Two-Dimensional Bismuth Chalcogenide Nanoplates. *Nat. Commun.* **2014**, *5* (1), 1–7. https://doi.org/10.1038/ncomms6670.

(53) Bao, W.; Wan, J.; Han, X.; Cai, X.; Zhu, H.; Kim, D.; Ma, D.; Xu, Y.; Munday, J. N.; Drew, H. D.; Fuhrer, M. S.; Hu, L. Approaching the Limits of Transparency and Conductivity in Graphitic Materials through Lithium Intercalation. *Nat. Commun.* **2014**, *5* (1), 1–9. https://doi.org/10.1038/ncomms5224.

(54) Kulish, V. V.; Manzhos, S. Comparison of Li, Na, Mg and Al-Ion Insertion in Vanadium Pentoxides and Vanadium Dioxides. *RSC Adv.* **2017**, *7* (30), 18643–18649. https://doi.org/10.1039/C7RA02474F.

(55) Wang, W.; Jiang, B.; Xiong, W.; Sun, H.; Lin, Z.; Hu, L.; Tu, J.; Hou, J.; Zhu, H.; Jiao, S. A New Cathode Material for Super-Valent Battery Based on Aluminium Ion Intercalation and Deintercalation. *Sci. Rep.* **2013**, *3* (1), 1–6. https://doi.org/10.1038/srep03383.

(56) Luo, T.; Liu, Y.; Su, H.; Xiao, R.; Huang, L.; Xiang, Q.; Zhou, Y.; Chen, C. Nanostructured-VO2(B): A High-Capacity Magnesium-Ion Cathode and Its Electrochemical Reaction Mechanism. *Electrochim. Acta* **2018**, *260*, 805–813. https://doi.org/10.1016/J.ELECTACTA.2017.12.042.

Supporting Information

Modulation of phase transition properties in VO_2(B) and VO_2(M) films via lithium intercalation

Zihao He[1,§], Zhimin Qi[2,§], Bo Yang[2], Ping Lu[3], Jianan Shen[2], Neil Dilley[4], Xinghang Zhang[2], Haiyan Wang[1,2]*

[1]School of Electrical and Computer Engineering, Purdue University, West Lafayette, IN 47907, United States

[2]School of Materials Engineering, Purdue University, West Lafayette, IN 47907, United States
[3]Sandia National Laboratories, Albuquerque, NM, 87185, United States
[4]Birck Nanotechnology Center, Purdue University, West Lafayette, IN 47907, USA

*Author to whom correspondence should be addressed. E-mail: hwang00@purdue.edu

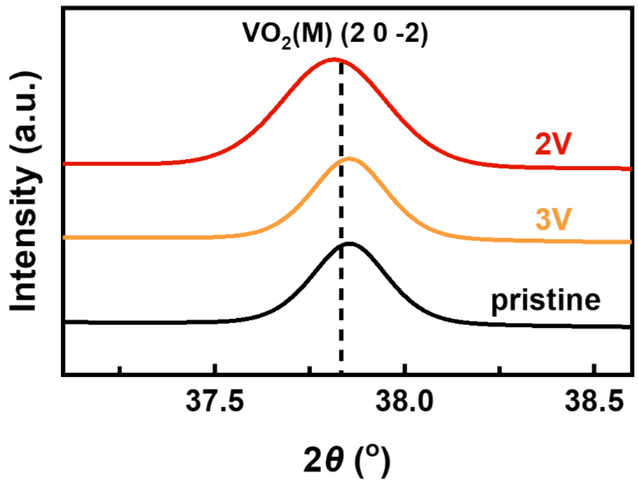

Figure S1. Local XRD *θ-2θ* scan of the pristine, 3V, and 2V lithiated VO_2(B) films on SRO-buffered STO substrates. The results indicate the existence of VO_2(M) phase within the film.

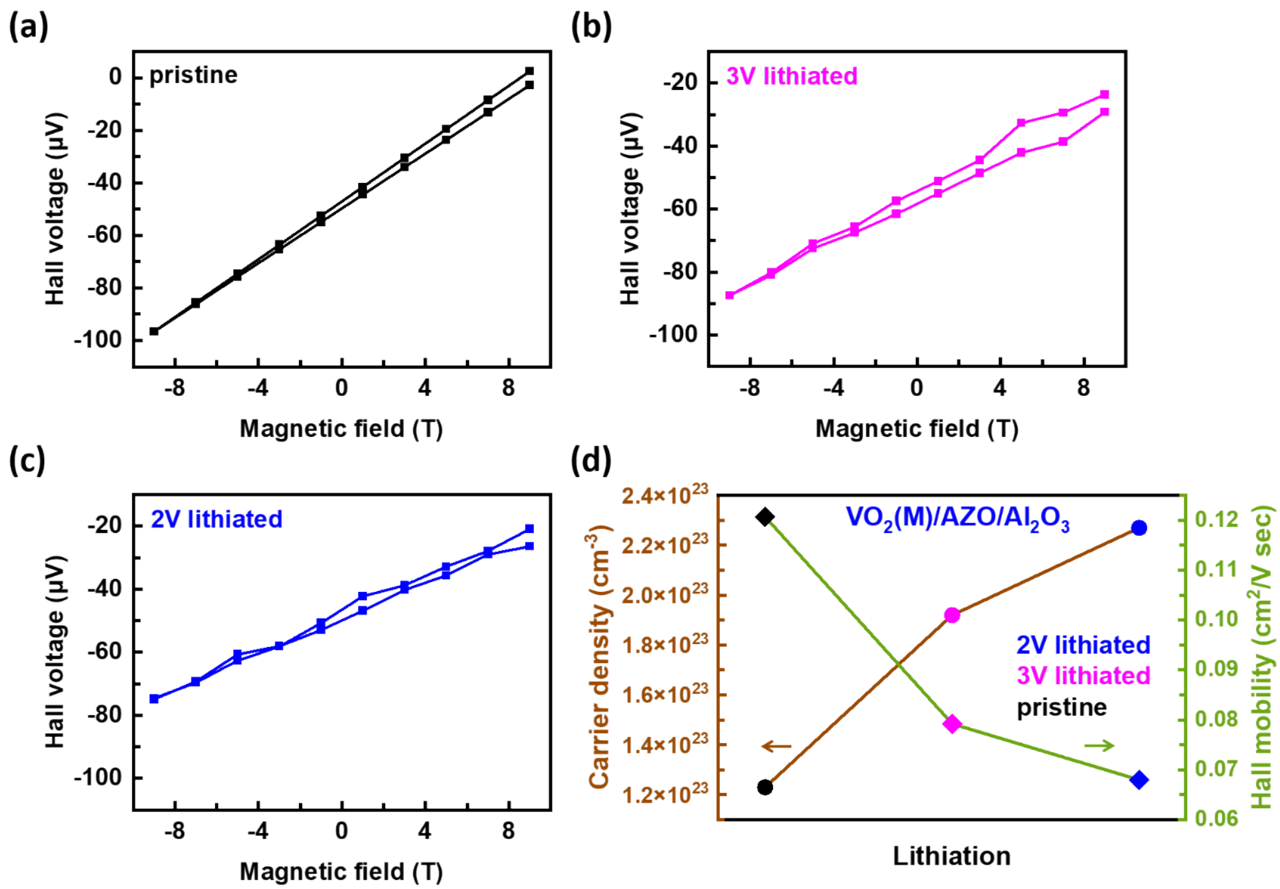

Figure S2. Hall-effect measurement of (a) the pristine; (b) 3V lithiated; and (c) 2V lithiated VO_2(M) films on AZO-buffered c-cut sapphire. (d) The electron carrier concentration and the hall mobility in pristine and lithiated VO_2(M) films at 380 K as a function of the lithiation voltage.

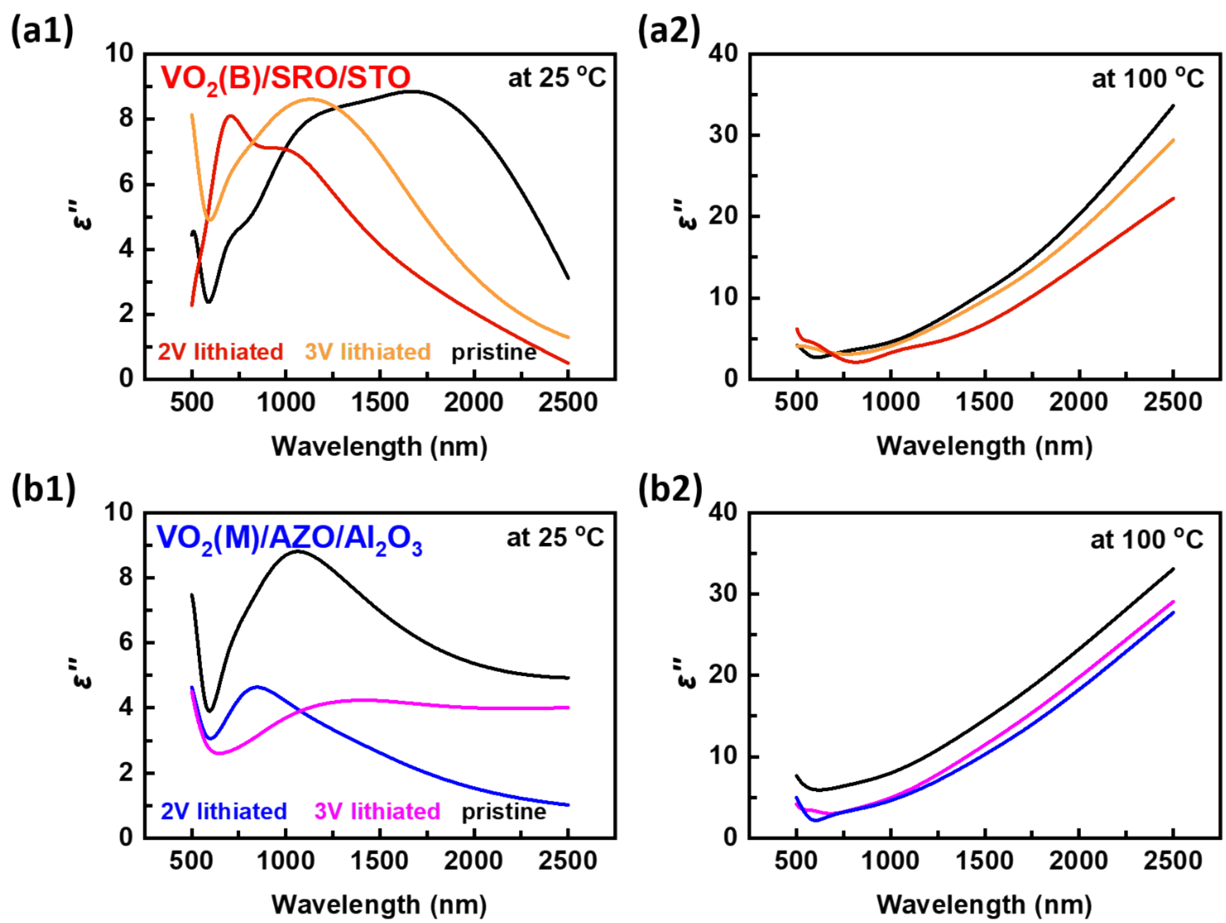

Figure S3. The dielectric permittivity *ε'* (imaginary part) (a1) at 25 °C and (a2) at 100 °C for the pristine, 3V, and 2V lithiated VO_2(B) films. The dielectric permittivity *ε'* (imaginary part) (b1) at 25 °C and (b2) at 100 °C for the pristine, 3V, and 2V lithiated VO_2(M) films.

TOC GRAPHICS